Science Advances
AAAS

advances.sciencemag.org/cgi/content/full/6/51/eabb7171/DC1

Supplementary Materials for

Rewritable color nanoprints in antimony trisulfide films

Hailong Liu, Weiling Dong, Hao Wang, Li Lu, Qifeng Ruan, You Sin Tan, Robert E. Simpson*, Joel K. W. Yang*

*Corresponding author. Email: robert_simpson@sutd.edu.sg (R.E.S.); joel_yang@sutd.edu.sg (J.K.W.Y.)

Published 16 December 2020, *Sci. Adv.* **6**, eabb7171 (2020)
DOI: 10.1126/sciadv.abb7171

This PDF file includes:

Section S1. Additional optical simulations and measurements.

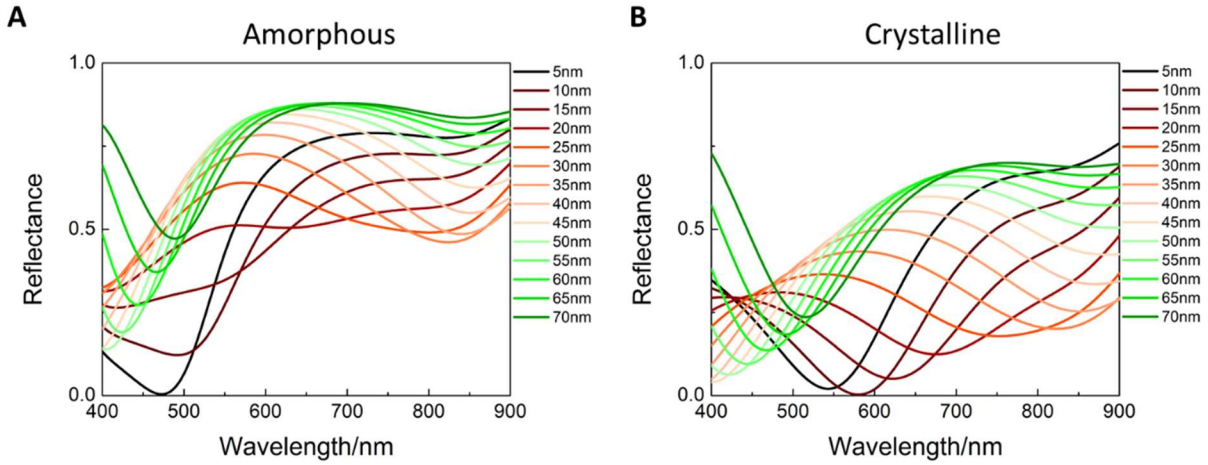

Fig. S1. Effect of Si_3N_4 thickness on the reflectance spectra of the 20 nm device. The simulated reflectance spectra of the amorphous (**A**) and crystalline (**B**) device with 20 nm Sb_2S_3 with simultaneously varying the thicknesses of both the top and bottom Si_3N_4 from 5 to 70 nm. The optimum thickness for Si_3N_4 is 5 nm.

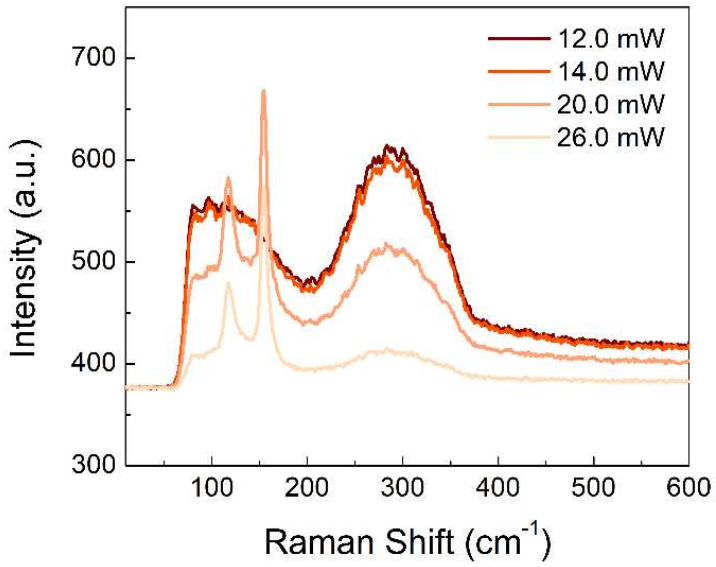

Fig. S2. Raman spectra of the device with laser power larger than 12.0 mW. Raman spectra of our four-layer device (20 nm Sb_2S_3) with laser power higher than 12.0 mW. It shows that the Sb_2S_3 is damaged when the laser power is larger than 20.0 mW.

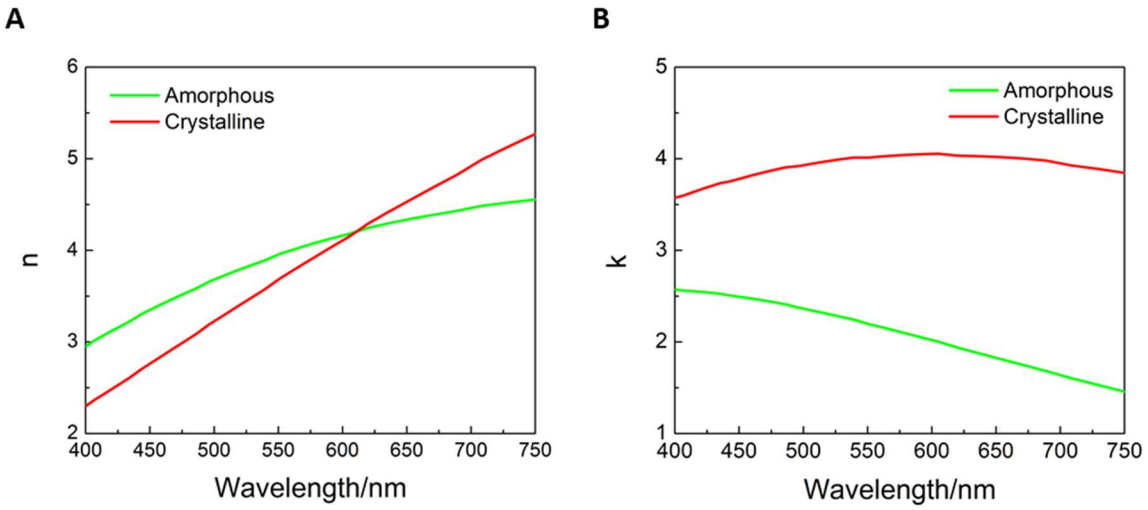

Fig. S3. Measured optical constants of $Ge_2Se_2Tb_5$. Measured refractive index (**A**) and extinction coefficient (**B**) of $Ge_2Se_2Tb_5$ in amorphous and crystalline in the visible region.

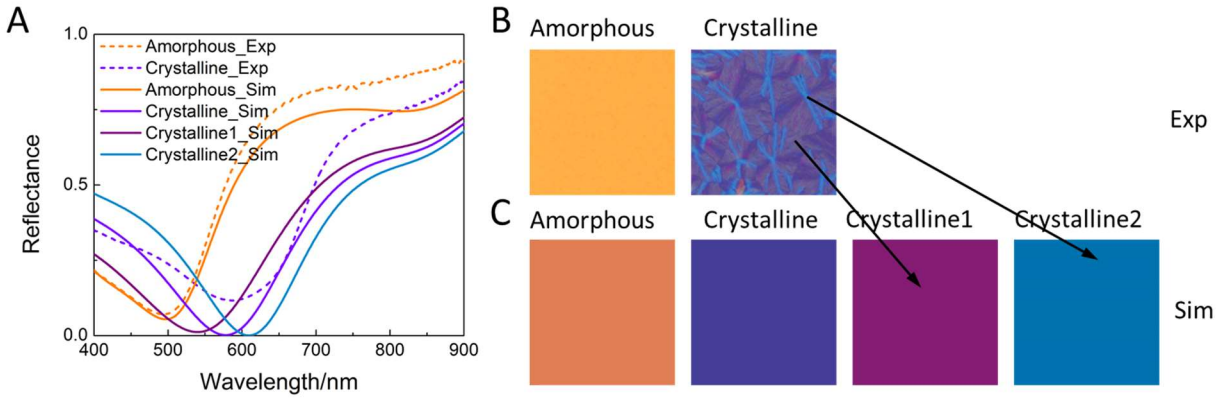

Fig. S4. Reflectance and color for amorphous and crystalline devices with 20 nm Sb_2S_3 films. (**A**) Simulated reflectance spectra of the device with 20 nm Sb_2S_3, and the measured refractive indices of amorphous, crystalline 1 and crystalline 2 in Fig. 2 are employed for the simulations. The refractive index of crystalline for simulation is the average of that for crystalline 1 and 2. (**B**) Bright-field micrographs of the amorphous and crystalline color patches of the device with 20 nm Sb_2S_3. (**C**) Simulated color patches for the device at amorphous, crystalline (average), crystalline1, and crystalline2 states.

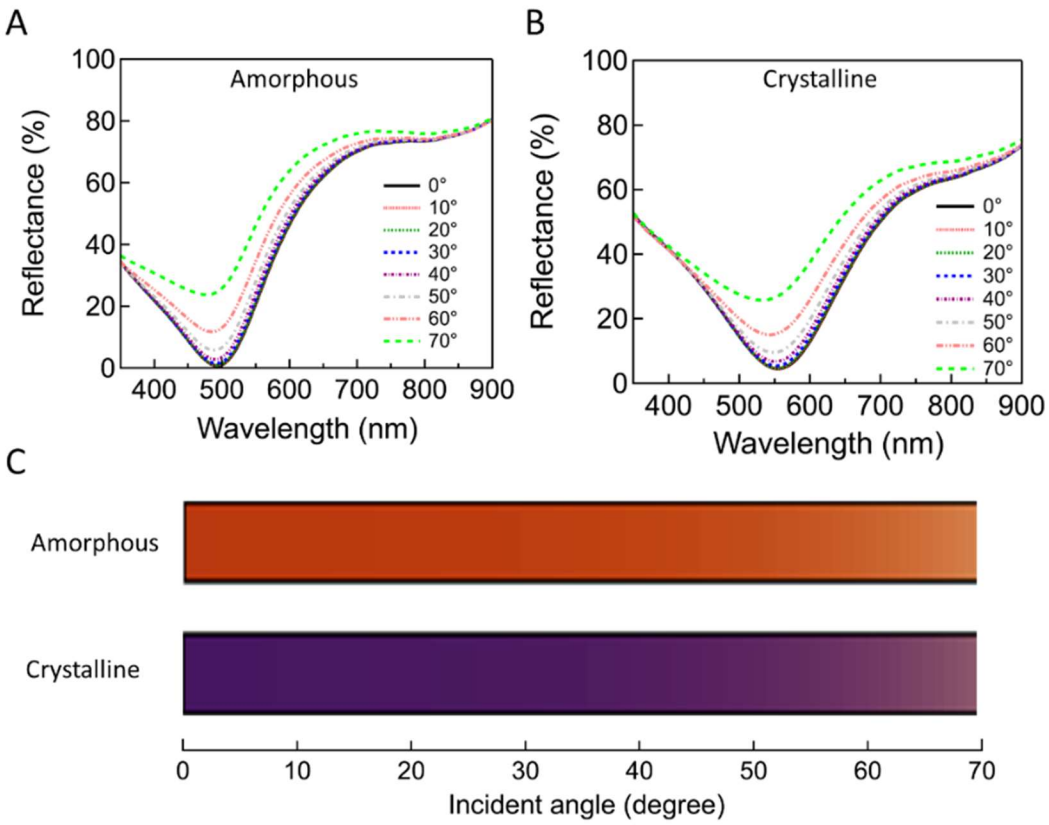

Fig. S5. Angle-independent colors of the amorphous and crystalline structures. Calculated reflectance spectra as a function of angle of incidence for amorphous (**A**) and crystalline (**B**) Si_3N_4(5 nm)/Sb_2S_3(20 nm)/Si_3N_4(5 nm)/Al(100 nm) structures. (**C**) Effect of incident angle (0° - 70°) on the color change of the amorphous and crystalline structures.

An optical thin-film multilayer model can be employed to explain the reflectance of our structures. When the light is incident on the surface of our structure (Si_3N_4/Sb_2S_3/Si_3N_4/Al), the beam is split into two parts, i.e. a reflected beam (r_1) and a transmitted beam (t_1) that enters the Sb_2S_3. The transmitted beam (t_1) in Sb_2S_3 is also split into two parts (reflected r_2 and transmitted beam t_2) at the interface of Sb_2S_3/Si_3N_4. Part of the reflected beam (r_2) is transmitted out to the surface of the nanostructures and interferes with r_1. Multiple reflections and transmissions will take place at each interface. The reflected beam r_1 interferences with all the light reflected out of the Si_3N_4/Sb_2S_3/Si_3N_4/Al structure to form a complex reflectance coefficient for each wavelength of light. The square of the amplitude of the complex reflectance coefficient for each wavelength represents the reflectivity. For each layer film, the reflection and transmission efficiency at each interface are related to the refractive index (n + ik), layer thickness and wavelength of light. The n and k for amorphous and crystalline Sb_2S_3 are substantially changed, which leads to different reflectance (or absorption, i.e. 1-Reflectivity) for each wavelength of light propagating within it. Therefore, the resonance of the structure can be tuned through switching the phase state of Sb_2S_3.

In our stack structures, we employ the multilayer thin film model to calculate the complex reflectance coefficient (***r***) as a function of the thickness of the structure for amorphous and crystalline states, as shown in Fig. S6. We started by calculating complex reflectance coefficient from the Si substrate, as we build up the thin film stack from the bottom Al layer to the top Si_3N_4 layer. For the amorphous state in Fig. S6A, we select the wavelength at the resonance as 498 nm, and the calculated reflectance coefficient is started from $\boldsymbol{r} = -0.6 + 0j$ for Si substrate. With increasing the thickness of the Al film to 100 nm, the reflectance ($|\boldsymbol{r}|$) is ~1. With increasing the thickness of Sb_2S_3, the reflection coefficient is gradually decreased to $\boldsymbol{r} = 0.1 + 0.25j$. After adding the top Si_3N_4, the reflection coefficient is almost $\boldsymbol{r} = 0 + 0j$, which corresponds to the maximum absorption and minimum reflectance of the structure. Fig. S6B shows the corresponding complex reflectance coefficient for the crystalline structure at 498 nm. Notably, the topmost surface at the air/Si_3N_4 interface has a reflectance $\boldsymbol{r} = -0.4 + 0.02j$, in agreement with the measured spectra. Fig. S6C shows the complex reflectance coefficient of the crystalline structure at its resonance dip, and the coefficient map displays a minimum reflectivity at the surface of the structure.

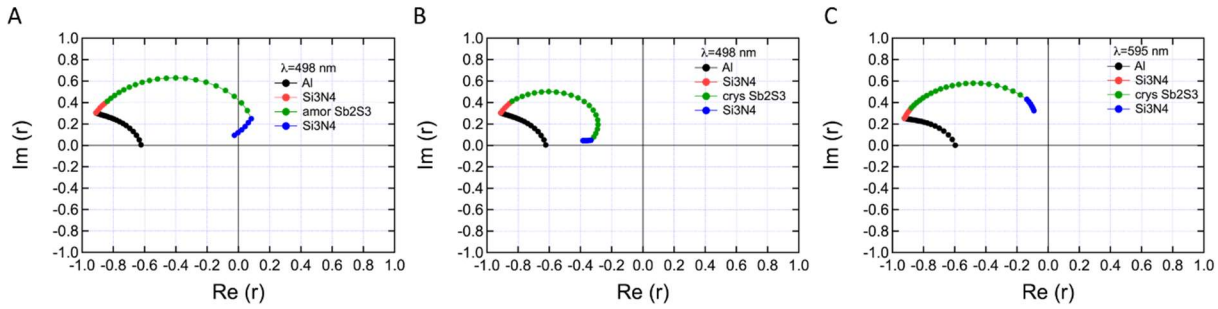

Fig. S6. The complex reflection coefficient of the $Si_3N_4/Sb_2S_3/Si_3N_4$/Al as a function of thickness of each layer. (**A**) Amorphous structure at 498 nm. Crystalline structure at 498 (**B**) and 595 nm (**C**).

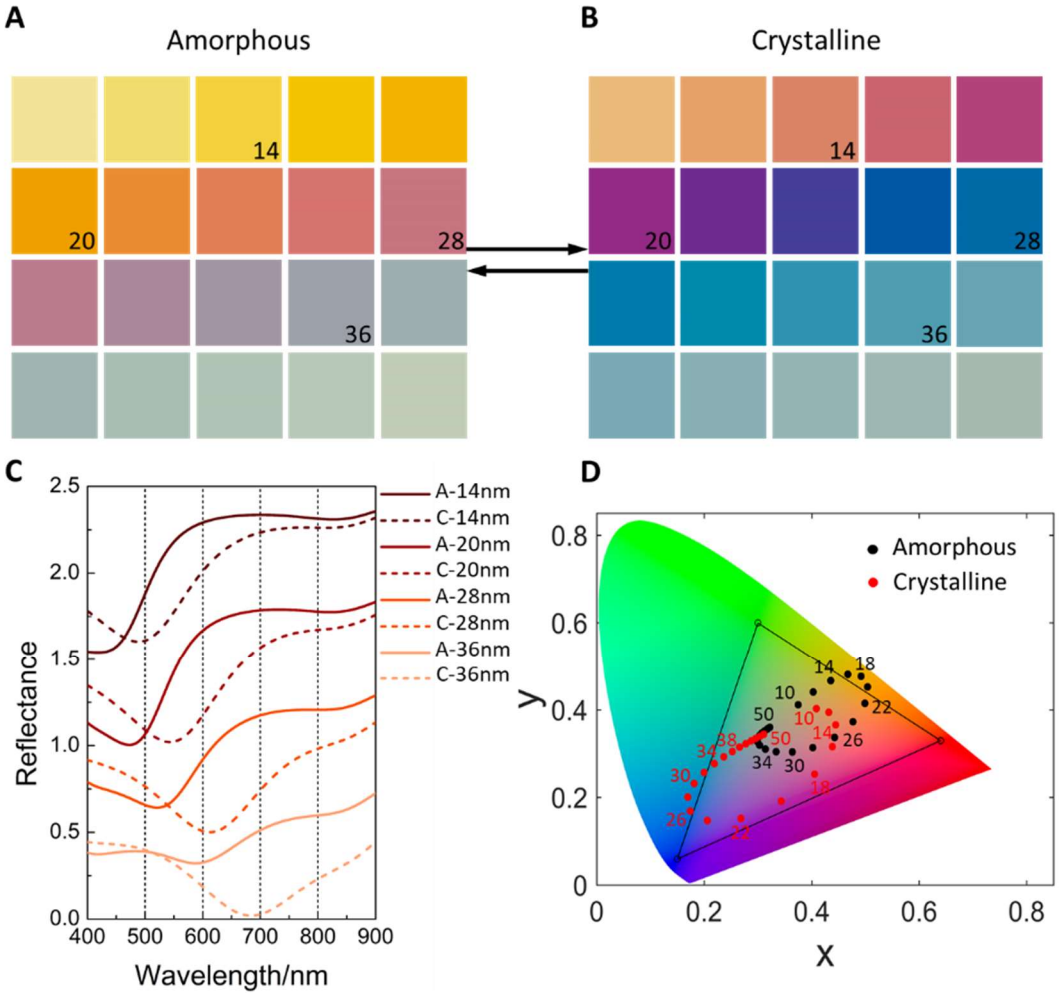

Fig. S7. Calculated amorphous (A) and crystalline (B) color palettes with varying the thickness *t* of Sb_2S_3 from 10 to 50 nm. (**C**) Simulated reflectance spectra of the device. (**D**) CIE chromaticity diagram of the devices with the thickness of Sb_2S_3 film varying from 10 to 50 nm.

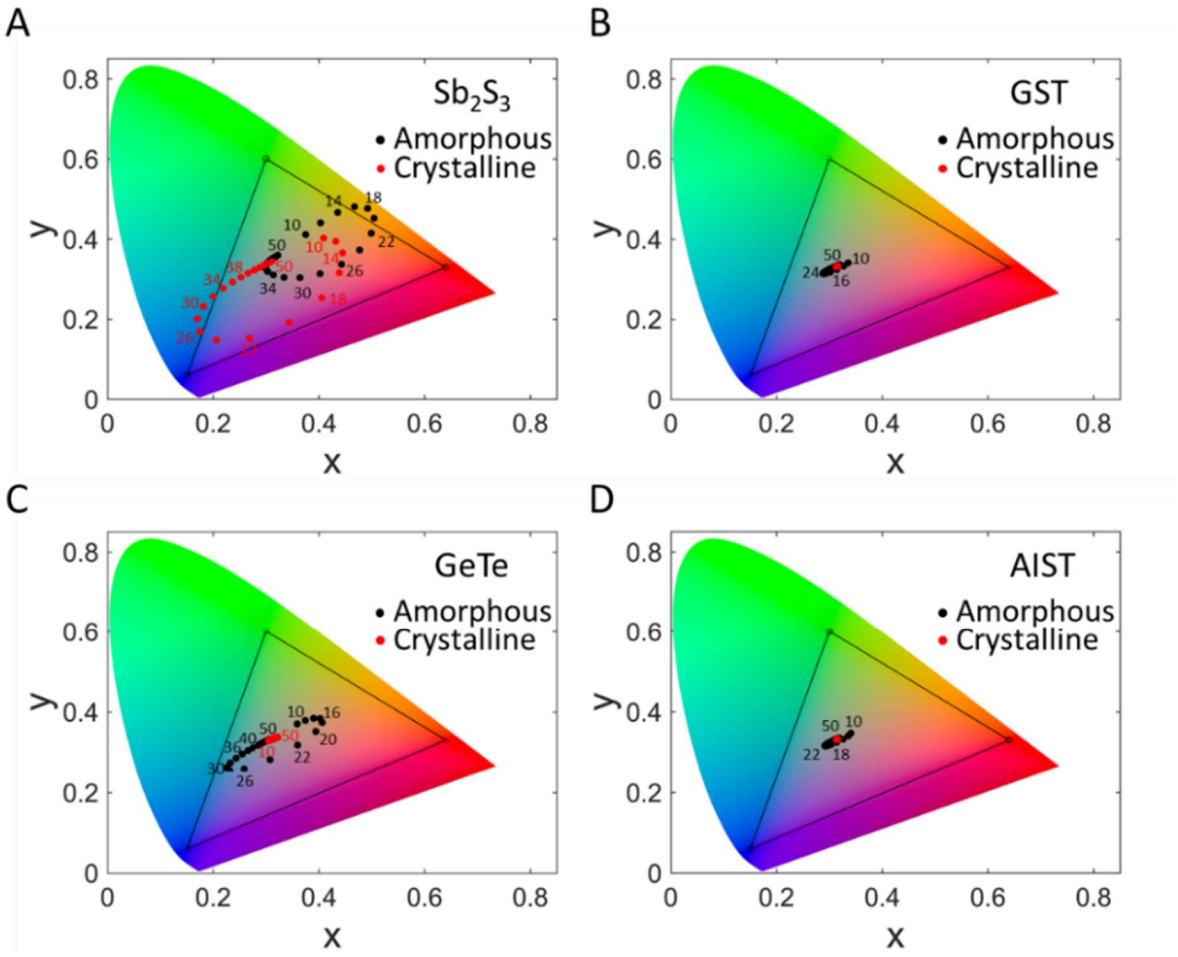

Fig. S8. CIE chromaticity diagrams of the device of Si_3N_4(5 nm)/PCM(t_{PCM} nm)/Si_3N_4(5 nm)/Al(100 nm) on a Si substrate. The PCM is Sb_2S_3 (**A**), $Ge_2Sb_2Te_5$ (GST, **B**), GeTe (**C**), and $Ag_3In_4Sb_{76}Te_{17}$ (AIST, **D**). The thickness (t_{PCM} nm) of PCM varied from 10 to 50 nm.

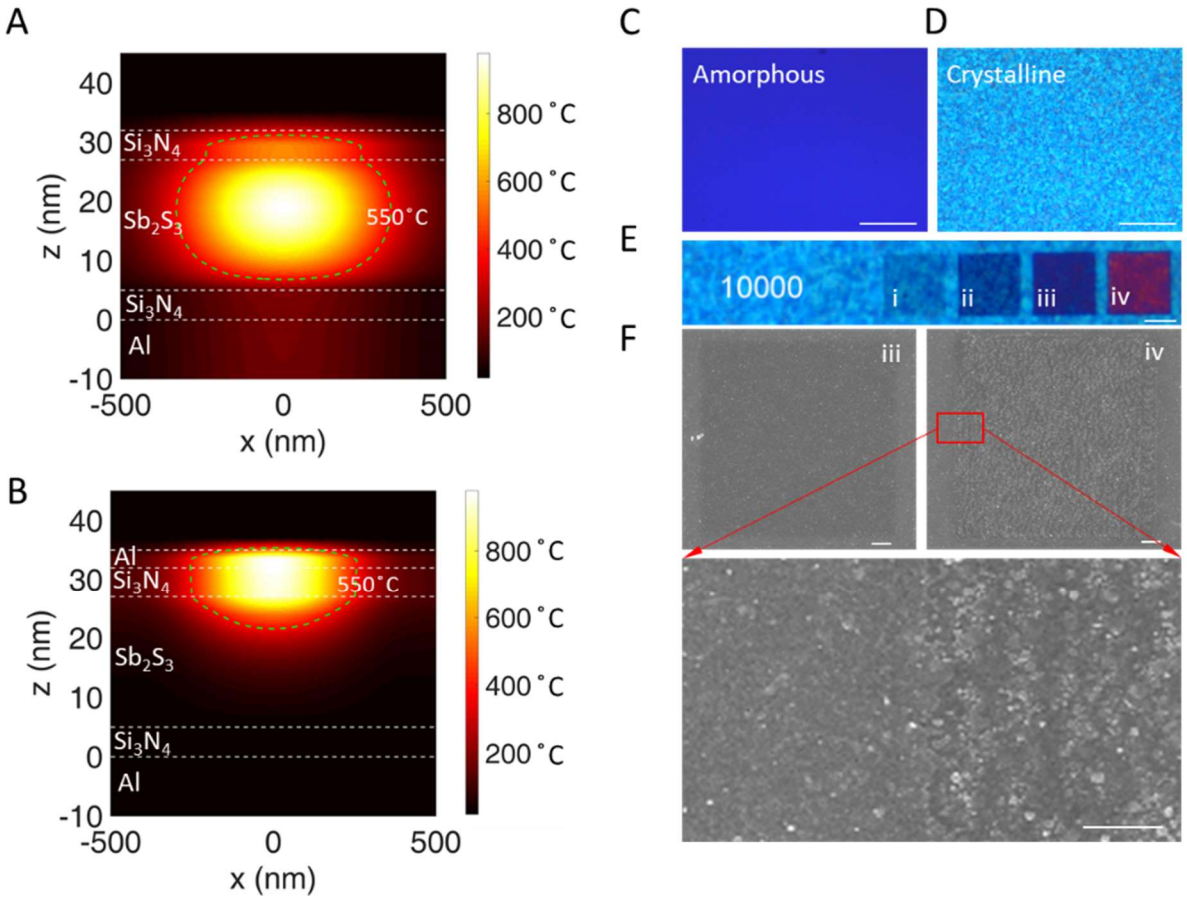

Fig. S9. Thermal simulations and re-amorphization experiments for the structure with top Al film. Calculated cross-sectional temperature distributions within Si_3N_4(5 nm)/Sb_2S_3(20 nm)/Si_3N_4(5 nm)/Al(100 nm) (**A**) and Al(3 nm)/Si_3N_4(5 nm)/Sb_2S_3(20 nm)/Si_3N_4(5 nm)/Al(100 nm) (**B**). Optical micrographs of the structures with 3 nm Al on the top surface at amorphous (**C**) and crystalline states (**D**). (**E**) Re-amorphization of the film with top Al at different laser powers (i) 2.0, (ii) 4.0, (iii) 6.0, (iv) 8.0 mW. (**F**) SEM images of the re-amorphized areas of (iii) and (iv). High magnification SEM image showing damage to the top Al film. Scale bars: 50 µm (C, D), 5 µm (E), 1 µm (F).

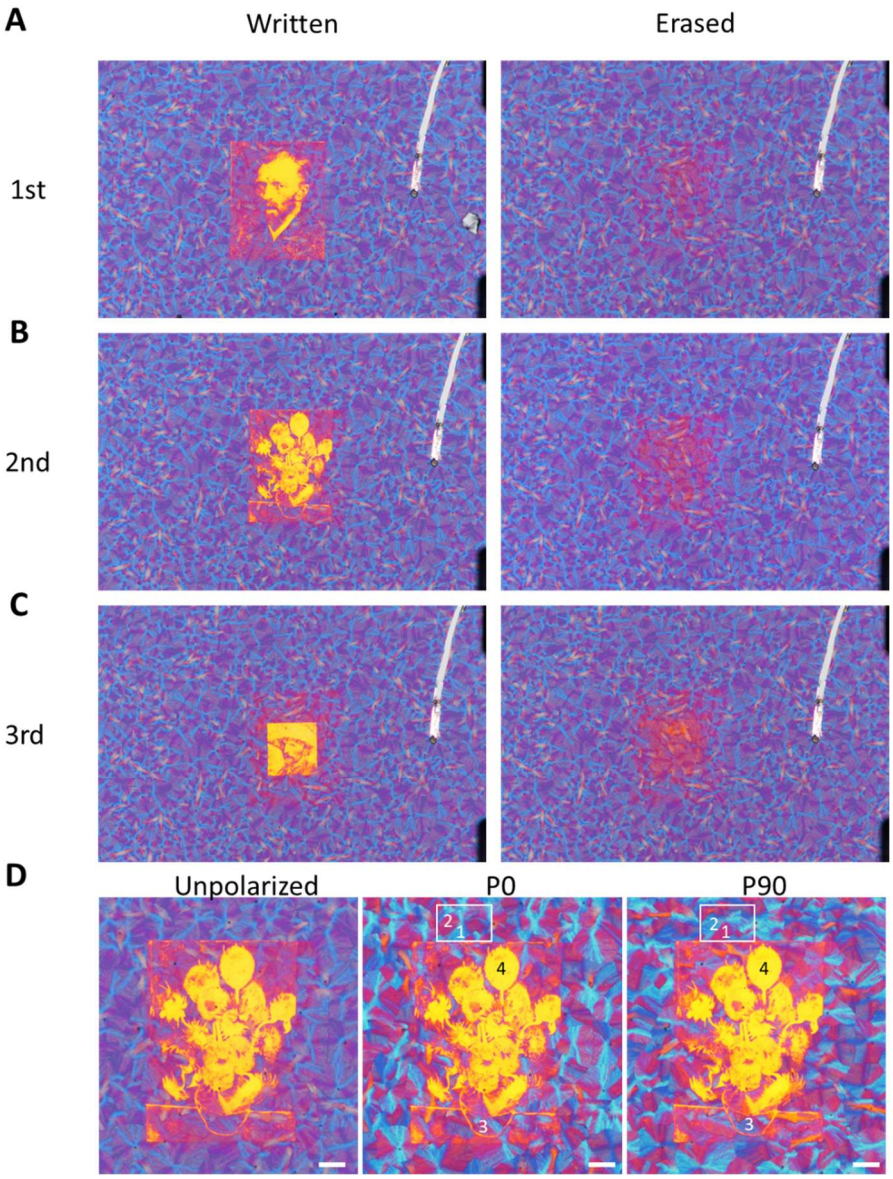

Fig. S10. Rewritable color prints with markers. (**A**) Optical micrographs of the same region of sample with 20 nm Sb_2S_3 showing the self-portrait painting of Vincent van Gogh (left) and the erased sample in crystalline state after thermal annealing (right). (**B**) Print of The Vase with Fourteen Sunflowers of Vincent van Gogh patterned on the same area (left) and the erased same area (right). (**C**) A second self-portrait painting of Vincent van Gogh was written as the third image (left) and the erased sample (right). (**D**) Polarization-dependent color print. Optical micrographs of the same color print of The Vase with Fourteen Sunflowers of Vincent van Gogh's under unpolarized and mutually perpendicular polarizations. The background crystalline colors are polarization-dependent and switchable, as shown by the marked areas 1 and 2. Conversely, the re-amorphized area 4 are polarization-independent. The intermediate state, marked as area 3, is also polarization dependent. Scale bars: 20 μm.

Section S2. Thermal model for temperature distribution calculation.

The interaction process between pulsed laser and materials has been intensively studied and many interesting effects such as pressure variation, increased temperature confinement, vibration modes, bubble formation, nano-particle modification and acoustic wave generation have been triggered. The absorption of electromagnetic energy from the laser pulse is usually described as a three-step process. In the first step, part of the laser energy is absorbed by the electrons over a time scale of ~100 fs and Fermi-Dirac distribution can be used to depict the electronic state. Subsequently, through electron-phonon thermalization, also known as electron-lattice interaction, thermal equilibrium will be established, thus the temperature of electron and lattice will equilibrate, i.e., T_e=T_l. This process usually occurs in a time scale of several picoseconds. Finally, the energy diffusion to the surrounding medium lasts from several hundred of ps to a few ns, which can overlap in time with the second step (*38*).

In the first step, the heat generation is governed by the Joule effect and can be calculated as

$$Q = \int_V q(\boldsymbol{r}) d^3 r \tag{1}$$

where, V is the volume of the heat absorption material, $q(\mathbf{r})$ is the heating power density. Considering the property of time-harmonic electromagnetic field, $q(\mathbf{r})$ can be expressed as (*39*)

$$q(\boldsymbol{r}) = \frac{1}{2} Re[\boldsymbol{J}^*(\boldsymbol{r}) \cdot \boldsymbol{E}(\boldsymbol{r})] \tag{2}$$

in which, $\mathbf{J}(\mathbf{r})$ and $\mathbf{E}(\mathbf{r})$ are the complex amplitudes of the electronic current density and complex electric field, respectively. Thus, combined with the relation of current and electromagnetic polarization, we obtain

$$q(\boldsymbol{r}) = \frac{1}{2} \omega \, Im\big(\varepsilon(\omega)\big) \, \varepsilon_0 |\boldsymbol{E}(\boldsymbol{r})|^2 \tag{3}$$

where, ω is the frequency of electromagnetic wave, $\varepsilon(\omega)$ is the complex permittivity of material, ε_0 is the vacuum permittivity.

Generally, according to the L'Hôpital's rule, the energy distribution of an incident single laser pulse can be expressed by a two-dimensional Gaussian function as

$$F_l(r) = \frac{2P_0}{\pi {\omega_r}^2 f_r} exp\left(-\frac{2r^2}{{\omega_r}^2}\right) \tag{4}$$

here, P_0 is the average incident laser power, f_r is the pulse frequency and ω_r is the pulse waist. Taking the pulse duration into consideration, the laser power fluence is

$$F_l(r,t) = \frac{2P_0}{\pi {\omega_r}^2 f_r} \frac{1}{\sqrt{\pi}\tau} exp\left(-\frac{2r^2}{{\omega_r}^2}\right) exp\left(-\frac{(t-t_0)^2}{\tau^2}\right) \tag{5}$$

in which, time duration

$$\tau = \frac{t_{pulse-widt}}{2\sqrt{ln\,2}} \tag{6}$$

and t_0=2τ, thus t= 0 fs corresponds to the beginning of the laser pulse and the pulse intensity reaches maximum at t_0. Therefore, the investigated system absorbs the energy from the incident laser pulse

with a Gaussian profile as a function of time and a 2D Gaussian profile in spatial domain. The specific absorbed energy can be obtained by solving Maxwell equations.

Since the laser pulse duration is much shorter than the thermal equilibrium time for the electron and lattice, a two-temperature model (TTM) is applied to describe the non-equilibrium thermal phenomena in the system:

$$C_e \frac{\partial T_e}{\partial t} = \nabla(k_e \nabla T_e) - G(T_e - T_l) + Q$$
$$C_l \frac{\partial T_l}{\partial t} = \nabla(k_l \nabla T_l) + G(T_e - T_l) \quad (7)$$

here, $C_l = \rho C_p$ is the heat capacity of lattice, ρ is the density of material, C_p is the heat capacity at constant pressure, k_e and k_l are the thermal conductivity of electron and lattice, respectively. C_e is the heat capacity of the electron distribution,

$$C_e = \frac{\pi^2 n_e k_B}{2\mu_F} T_e \quad (8)$$

in which, n_e is the density of electrons, k_B is the Boltzmann constant, μ_F is the Fermi energy. G is the electron-phonon coupling factor that represents the exchange speed of thermal energy between electrons and phonons. During the thermal equilibrium process of the electron and lattice, thermal diffusion to the surrounding occurs, finally leading to heat dissipation to the system.

To simulate the femtosecond laser pulse interaction with our designed system, an Electromagnetic Two-Temperature Model (EM-TTM) was developed by employing the commercial finite element method (FEM) software COMSOL Multiphysics based on the theory described above. The wavelength of laser pulse is 780 nm with pulse rate 80 MHz and pulse Full width at half maximum (FWHM) 100 fs. The permittivity (ε) and thermal properties of the materials are obtained from built-in material library in COMSOL and experimental measurement as following:

Thermal conductivity is 1.16 W/m·K, density is 4.6 g/cm^3, electrical conductivity 3.3×10^{-8} S/cm, lattice heat capacity is from Ref. *40*, the electron heat capacity is chosen as three orders of magnitude smaller than the lattice heat capacity, and electron-photon coupling strength is chosen as ~10^{17} W/(m^3·K). Experimental refractive index is 3.11 + 0.29 *i* for wavelength 780 nm.

REFERENCES AND NOTES

1. X. Zhu, C. Vannahme, E. Højlund-Nielsen, N. A. Mortensen, A. Kristensen, Plasmonic colour laser printing. *Nat. Nanotechnol.* **11**, 325–329 (2016).

2. K. Kumar, H. Duan, R. S. Hegde, S. C. W. Koh, J. N. Wei, J. K. W. Yang, Printing colour at the optical diffraction limit. *Nat. Nanotechnol.* **7**, 557–561 (2012).

3. Y. Jin, I. Qamar, M. Wessely, A. Adhikari, K. Bulovic, P. Punpongsanon, S. Mueller, Photo-chromeleon: Re-programmable multi-color textures using photochromic dyes, in *Proceedings of the 32nd Annual ACM Symposium on User Interface Software and Technology* (ACM, 2019), pp. 701–712.

4. S. J. Tan, L. Zhang, D. Zhu, X. M. Goh, Y. M. Wang, K. Kumar, C.-W. Qiu, J. K. W. Yang, Plasmonic color palettes for photorealistic printing with aluminum nanostructures. *Nano Lett.* **14**, 4023–4029 (2014).

5. H. Liu, J. Xu, H. Wang, Y. Liu, Q. Ruan, Y. Wu, X. Liu, J. K. W. Yang, Tunable resonator-upconverted emission (TRUE) color printing and applications in optical security. *Adv. Mater.* **31**, 1807900 (2019).

6. Z. Dong, J. Ho, Y. F. Yu, Y. H. Fu, R. Paniagua-Dominguez, S. Wang, A. I. Kuznetsov, J. K. W. Yang, Printing beyond sRGB color gamut by mimicking silicon nanostructures in free-space. *Nano Lett.* **17**, 7620–7628 (2017).

7. Y. Liu, H. Wang, J. Ho, R. C. Ng, R. J. H. Ng, V. H. Hall-Chen, E. H. H. Koay, Z. Dong, H. Liu, C.-W. Qiu, J. R. Greer, J. K. W. Yang, Structural color three-dimensional printing by shrinking photonic crystals. *Nat. Commun.* **10**, 4340 (2019).

8. H. Kim, J. Ge, J. Kim, S.-e. Choi, H. Lee, H. Lee, W. Park, Y. Yin, S. Kwon, Structural colour printing using a magnetically tunable and lithographically fixable photonic crystal. *Nat. Photonics* **3**, 534–540 (2009).

9. M. A. Kats, R. Blanchard, P. Genevet, F. Capasso, Nanometre optical coatings based on strong interference effects in highly absorbing media. *Nat. Mater.* **12**, 20–24 (2013).

10. Y. M. Andreeva, V. C. Luong, D. S. Lutoshina, O. S. Medvedev, V. Y. Mikhailovskii, M. K. Moskvin, G. V. Odintsova, V. V. Romanov, N. N. Shchedrina, V. P. Veiko, Laser coloration of metals in visual art and design. *Opt. Mater. Express* **9**, 1310–1319 (2019).

11. P. Hosseini, C. D. Wright, H. Bhaskaran, An optoelectronic framework enabled by low-dimensional phase-change films. *Nature* **511**, 206–211 (2014).

12. C. Ríos, P. Hosseini, R. A. Taylor, H. Bhaskaran, Color depth modulation and resolution in phase-change material nanodisplays. *Adv. Mater.* **28**, 4720–4726 (2016).

13. H.-K. Ji, H. Tong, H. Qian, N. Liu, M. Xu, X.-S. Miao, Color printing enabled by phase change materials on paper substrate. *AIP Adv.* **7**, 125024 (2017).

14. S. Yoo, T. Gwon, T. Eom, S. Kim, C. S. Hwang, Multicolor changeable optical coating by adopting multiple layers of ultrathin phase change material film. *ACS Photonics* **3**, 1265–1270 (2016).

15. R. E. Simpson, P. Fons, A. V. Kolobov, T. Fukaya, M. Krbal, T. Yagi, J. Tominaga, Interfacial phase-change memory. *Nat. Nanotechnol.* **6**, 501–505 (2011).

16. K. Chaudhary, M. Tamagnone, X. Yin, C. M. Spägele, S. L. Oscurato, J. Li, C. Persch, R. Li, N. A. Rubin, L. A. Jauregui, K. Watanabe, T. Taniguchi, P. Kim, M. Wuttig, J. H. Edgar, A. Ambrosio, F. Capasso, Polariton nanophotonics using phase-change materials. *Nat. Commun.* **10**, 4487 (2019).

17. Q. Wang, E. T. F. Rogers, B. Gholipour, C.-M. Wang, G. Yuan, J. Teng, N. I. Zheludev, Optically reconfigurable metasurfaces and photonic devices based on phase change materials. *Nat. Photonics* **10**, 60–65 (2016).

18. W. Dong, H. Liu, J. K. Behera, L. Lu, R. J. H. Ng, K. V. Sreekanth, X. Zhou, J. K. W. Yang, R. E. Simpson, Wide bandgap phase change material tuned visible photonics. *Adv. Funct. Mater.* **29**, 1806181 (2019).

19. L. Shao, X. Zhuo, J. Wang, Advanced plasmonic materials for dynamic color display. *Adv. Mater.* **30**, 1704338 (2018).

20. D. Franklin, Y. Chen, A. Vazquez-Guardado, S. Modak, J. Boroumand, D. Xu, S.-T. Wu, D. Chanda, Polarization-independent actively tunable colour generation on imprinted plasmonic surfaces. *Nat. Commun.* **6**, 7337 (2015).

21. H. You, A. Steckl, Three-color electrowetting display device for electronic paper. *Appl. Phys. Lett.* **97**, 023514 (2010).

22. S. Shang, Q. Zhang, H. Wang, Y. Li, Fabrication of magnetic field induced structural colored films with tunable colors and its application on security materials. *J. Colloid Interf. Sci.* **485**, 18–24 (2017).

23. H. Cho, S. Han, J. Kwon, J. Jung, H.-J. Kim, H. Kim, H. Eom, S. Hong, S. H. Ko, Self-assembled stretchable photonic crystal for a tunable color filter. *Opt. Lett.* **43**, 3501–3504 (2018).

24. X. Duan, S. Kamin, N. Liu, Dynamic plasmonic colour display. *Nat. Commun.* **8**, 14606 (2017).

25. M. Huang, A. J. Tan, F. Büttner, H. Liu, Q. Ruan, W. Hu, C. Mazzoli, S. Wilkins, C. Duan, J. K. W. Yang, G. S. D. Beach, Voltage-gated optics and plasmonics enabled by solid-state proton pumping. *Nat. Commun.* **10**, 5030 (2019).

26. G. J. Stec, A. Lauchner, Y. Cui, P. Nordlander, N. J. Halas, Multicolor electrochromic devices based on molecular plasmonics. *ACS Nano* **11**, 3254–3261 (2017).

27. W. Wang, N. Xie, L. He, Y. Yin, Photocatalytic colour switching of redox dyes for ink-free light-printable rewritable paper. *Nat. Commun.* **5**, 5459 (2014).

28. X. Zhu, W. Yan, U. Levy, N. A. Mortensen, A. Kristensen, Resonant laser printing of structural colors on high-index dielectric metasurfaces. *Sci. Adv.* **3**, e1602487 (2017).

29. J.-M. Guay, A. C. Lesina, G. Côté, M. Charron, D. Poitras, L. Ramunno, P. Berini, A. Weck, Laser-induced plasmonic colours on metals. *Nat. Commun.* **8**, 16095 (2017).

30. A. S. Roberts, S. M. Novikov, Y. Yang, Y. Chen, S. B. Boroviks, J. Beermann, N. A. Mortensen, S. I. Bozhevolnyi, Laser writing of bright colors on near-percolation plasmonic reflector arrays. *ACS Nano* **13**, 71–77 (2019).

31. F.-Z. Shu, F.-F. Yu, R.-W. Peng, Y.-Y. Zhu, B. Xiong, R.-H. Fan, Z.-H. Wang, Y. Liu, M. Wang, Dynamic plasmonic color generation based on phase transition of vanadium dioxide. *Adv. Opt. Mater.* **6**, 1700939 (2018).

32. I. Efthimiopoulos, C. Buchan, Y. Wang, Structural properties of Sb_2S_3 under pressure: Evidence of an electronic topological transition. *Sci. Rep.* **6**, 24246 (2016).

33. R. G. A. Garcia, C. A. M. Avendaño, M. Pal, F. P. Delgado, N. R. Mathews, Antimony sulfide (Sb_2S_3) thin films by pulse electrodeposition: Effect of thermal treatment on structural, optical and electrical properties. *Mater. Sci. Semicond. Proc.* **44**, 91–100 (2016).

34. H.-K. Ji, H. Tong, H. Qian, Y.-J. Hui, N. Liu, P. Yan, X.-S. Miao, Non-binary colour modulation for display device based on phase change materials. *Sci. Rep.* **6**, 39206 (2016).

35. S. G.-C. Carrillo, L. Trimby, Y.-Y. Au, V. K. Nagareddy, G. Rodriguez-Hernandez, P. Hosseini, C. Ríos, H. Bhaskaran, C. D. Wright, A nonvolatile phase-change metamaterial color display. *Adv. Opt. Mater.* **7**, 1801782 (2019).

36. E. L. Gurevich, Y. Levy, S. V. Gurevich, N. M. Bulgakova, Role of the temperature dynamics in formation of nanopatterns upon single femtosecond laser pulses on gold. *Phys. Rev. B* **95**, 054305 (2017).

37. Ž. Živković, N. Štrbac, D. Živković, D. Grujičić, B. Boyanov, Kinetics and mechanism of Sb_2S_3 oxidation process. *Thermochim. Acta* **383**, 137–143 (2002).

38. M. Hu, G. V. Hartland, Heat dissipation for Au particles in aqueous solution: Relaxation time versus size. *J. Phys. Chem. B* **106**, 7029–7033 (2002).

39. A. O. Govorov, H. H. Richardson, Generating heat with metal nanoparticles. *Nano Today* **2**, 30–38 (2007).

40. T. B. Nasr, H. Maghraoui-Meherzi, N. Kamoun-Turki, First-principles study of electronic, thermoelectric and thermal properties of Sb_2S_3. *J. Alloy. Compd.* **663**, 123–127 (2016).